Multi-angle aerosol optical depth retrieval method based on improved surface reflectance

Lijuan Chen[1], Ren Wang[1], Ying Fei[2], Peng Fang[2],Yong Zha[2], Haishan Chen[1*]

[1]Key Laboratory of Meteorological Disaster, Ministry of Education (KLME)/Joint International

Research Laboratory of Climate and Environment Change (ILCEC)/Collaborative Innovation

Center on Forecast and Evaluation of Meteorological Disasters (CIC-FEMD), Nanjing University

of Information Science and Technology, Nanjing 210044, China

[2]Key Laboratory of Virtual Geographic Environment of Ministry of Education, Jiangsu Center for

Collaborative Innovation in Geographical Information Resource Development and Application,

College of Geographic Science, Nanjing Normal University, Nanjing 210023, China

Correspondence: Haishan Chen (haishan@nuist.edu.cn)

Abstract

Retrieval of terrestrial aerosol optical depth (AOD) has been a challenge for satellite Earth observations, mainly due to the difficulty of estimating surface reflectance caused by land-atmosphere coupling. Current satellite AOD retrieval products have low spatial resolution under complex surface processes. In this study, based on our previous studies of AOD retrieval, we further improved the estimation method of surface reflectance by establishing an error correction model, which helped us obtain more accurate AOD retrievals. We constructed a lookup table using the Second Simulation of Satellite Signal in the Solar Spectrum (6S) to achieve high-precision retrieval of AOD. The accuracy of the algorithm's retrieval was verified by AERONET (Aerosol Robotic Network) observations. The results indicated that the retrieved AOD

22 based on the improved method of this study has advantages in terms of fewer missing AOD pixels

23 and finer spatial resolution, compared to the MODIS AOD product and our previous estimation

24 method. Among the nine MISR angles, the optimal correlation coefficient (R) of retrieved AOD

25 and observed AOD can reach 0.89. Root mean square error (RMSE) and relative mean bias (RMB)

26 can reach minimum values of 0.20 and 0.32, respectively. This study will help to further improve

27 the accuracy of retrieving multi-angle AOD at large spatial scales and long time series.

29 Keywords: surface reflectance; aerosol optical depth; satellite remote sensing; MISR; MODIS

30 **1. Introduction**

31   Aerosols are liquid or solid particles suspended in the atmosphere, with particle diameters

32 ranging from approximately 0.001 to 100 μm (Giles et al., 2019). Aerosols have a significant

33 impact on the Earth's radiation budget balance, and estimating their uncertainties is challenging

34 (Holben et al., 2001; Li et al., 2020; Berhane et al., 2021; Sun et al., 2022). As a result, the direct

35 and indirect effects of aerosols have garnered widespread attention in the study of climate change

36 mechanisms (Hatzianastassiou et al., 2009; Dao et al., 2014; Daniel et al., 2014; Samset et al.,

37 2018; Li et al., 2018; Huang et al., 2021). Additionally, high concentrations of aerosols can pose a

38 serious threat to human health (Lee et al., 2010; Dehghani et al., 2012; Mironova et al., 2015). The

39 optical properties of aerosols include parameters such as aerosol optical depth (AOD), scattering

40 phase function, single scattering albedo, and absorbing optical depth. Among there, AOD is an

41 important parameter defined as the integral of aerosol extinction coefficient in the vertical

42 direction. It describes the attenuation effect of aerosols on light and serves as an important

43 indicator of air pollution levels. Over the past two decades, multi-channel spectrometers on

geostationary and polar orbit satellites have been utilized for AOD retrieval. The AOD products

obtained through satellite retrieval are widely employed in the study of atmospheric environment

(Kaufman et al, 1997; Xie et al., 2019; Chen et al., 2021). Although the accuracy of AOD retrieval

has continuously improved, there is still ample room for enhancing in the retrieval results over

land.

Scholars have conducted studies using multi-angle sensors. Flowerdew et al. (1996) utilized

Along-Track Scanning Radiometer 2 (ATSR-2) dual-angle observation data, based on the

approximate condition of minimum variation of surface reflectance with wavelength, and using

the assumption of independent invariance of ground features and Lambertian bodies. They

simulated this by using a bidirectional reflection radiation transfer model and proposed a

dual-angle algorithm (ATSR-DV) to retrieve AOD over land. Kokhanovsky et al. (2009) used the

ATSR-DV algorithm to retrieve the AOD over Germany on October 13, 2005, and compared the

retrieval results with MEdium-Resolution Imaging Spectrometer (MERIS) and MISR products.

They indicated that the ATSR-2 algorithm is also suitable for Advanced Along-Track Scanning

Radiometer (AATSR). Sundstrom et al. (2012) obtained an aerosol model of eastern China based

on Aerosol Robotic Network (AERONET) observation data and used the ATSR-DV algorithm to

retrieve the proportion of AOD and coarse to fine particles from AATSR data. Abdou et al. (2005)

compared the MISR AOD and the Moderate-resolution Imaging Spectroradiometer (MODIS)

AOD products carried by Terra using data from 62 AERONET observation sites. The results

showed that over land, the MODIS AOD in the 0.470 um and 0.660 um channels was 35% and

10% higher than MISR. In coastal and desert areas, the MODIS retrieval error was relatively large,

while over the ocean, in the 0.470 um and 0.660 um channels, the MISR was 0.1 and 0.05 higher

66 than the MODIS AOD value, respectively, mainly depends on the accuracy of radiometric

67 calibration. Martochik et al. (1997) proposed an algorithm for extracting aerosol optical

68 parameters using MISR multi-angle observations. The results showed that in the presence of dense

69 vegetation over land, AOD was extracted using its low reflectivity and multi-angle observations. If

70 dense vegetation did not exist, AOD and aerosol models were determined using the reflectance

71 function spectral contrast angle dependence relationship. As a new remote sensing tool,

72 multi-angle remote sensing has the ability to provide aerosol characteristics such as optical depth,

73 single scattering albedo, and phase function with sufficient precision, which is more suitable for

74 playing its unique role in aerosol research than traditional single-angle optical remote sensing

75 (Dubovik et al., 2019). Multi-angle remote sensing retrieval of aerosol optical properties can

76 utilize the angle information contained in satellite signals to better separate the contributions of the

77 surface and atmosphere, making it suitable for some bright surfaces. This provides a new approach

78 for AOD retrieval.

79   Surface reflectance measures the ability of land to absorb and reflect solar radiation. On land,

80 surface reflectance is relatively complex and is detected by satellite sensors after atmospheric

81 scattering and absorption. Satellite observations capture a combination of there two components,

82 making it challenging to directly separate surface reflectance from atmospheric scattering.

83 Consequently, the simultaneous retrieval of atmospheric aerosols and surface reflectance is a

84 primary goal in quantitative satellite remote sensing (Deuzé et al., 2001). In optical remote sensing,

85 the blue band has shorter wavelengths and low surface reflectivity, resulting in more reflection and

86 scattering caused by the atmosphere. Therefore, the blue band is commonly used for AOD

87 retrieval. During the AOD retrieval process, overestimating surface reflectivity leads to

88   underestimating AOD, while underestimating surface reflectance leads to overestimating AOD.

89   Separating atmospherically generated reflectance from surface reflectance in apparent reflectance

90   (reflectance at the top of the atmosphere) poses a challenge in AOD retrieval. Generally, aerosol

91   signals are weaker compared to surface signals (Dong et al., 2023). Previous studies have shown

92   that an intercept error of 0.01 in surface reflectance can result in a retrieval error of approximately

93   0.1 when using satellite remote sensing to retrieve AOD (Zhang et al., 2021). Therefore, accurate

94   estimates of surface reflectance are crucial for reliable aerosol retrieval.

95   A high-precision AOD product obtained from retrieval is of great significance for monitoring

96   changes in atmospheric pollution and providing decision-making support for pollution control.

97   Observing the spatial distribution of AOD is crucial for daily air pollution monitoring.

98   Additionally, aerosol particles can impact the energy balance between the land and the atmosphere

99   by absorbing and scattering solar radiation, thereby influencing the global climate system. To

100   enhance the accuracy and resolution of AOD retrieval, this study utilizes data from nine camera

101   angles in the blue band of MISR L1B2T from 2016 to 2018, employing an improved retrieval

102   algorithm. Firstly, the study analyzes the retrieval errors of MISR AOD for nine camera angles

103   prior to the implementation of the improved retrieval approach. Secondly, an error correction

104   model is established to rectify the estimated surface reflectance of MISR, thus improving the

105   surface reflectance at these nine angles. The improved surface reflectance retrieval is then used to

106   obtain highly accurate MISR AOD. Finally, the improved AOD retrieval method is validated, and

107   its estimated results are compared with the previous retrieval.

2. MISR, MODIS, and AERONET Data

2.1 MISR data

In this study, we utilized the MISR Level 1B2 Terrain Data (MI1B2T) and extracted the radiance data using the HEGTool (HDF-EOS To GeoTIFF Conversion Tool) software. We selected the corresponding blocks, output data types, and projection based on the regional location of the 180 radiation blocks and extracted the 64th and 65th blocks covering the Yangtze River Delta region (Figure S1). Moreover, we extracted the solar zenith angle, solar azimuth angle, satellite zenith angle, and satellite azimuth angle data for 9 cameras from the angle dataset (MI1B2GEOP) and selected the corresponding blocks, output data types, and projection information. To reduce the influence of clouds, we performed cloud detection and cloud pixel removal on satellite remote sensing images with cloud pixel coverage less than 50% and used a threshold value in the blue band to remove cloud pixels. However, through repeated experiments, we found that a fixed threshold could not effectively remove the cloud pixels from the 9 angles of the MISR sensor (Figures S2 and S3). Therefore, we adopted a dynamic threshold method to remove the cloud pixels from the MISR data. Details regarding the data used in this study can be found in Table S2.

2.2 MODIS data

In this study, we utilized MODIS L1B data, including radiance data (MOD02/MYD02) and geolocation data (MOD03/MYD03). The data preprocessing, including radiometric calibration, butterfly processing, geometric correction, reprojection, and band extraction, was conducted using the MODIS Conversion Toolkit (MCTK). The MODIS BRDF/Albedo is a standard Level-3

129 product representing surface properties derived from MODIS instruments onboard the Terra and

130 Aqua satellite platforms. This product has a 16-day retrieval period, and the observations from the

131 9th day of each 16-day cycle are weighted to generate daily data, known as the global daily

132 surface albedo product (Hsu et al., 2004). The core dataset for MODIS BRDF product is

133 MCD43A1.

134 **2.3 AERONET data**

135 This study utilized AERONET measurement stations, which employ CE-318 solar

136 radiometers produced in France. The instrument measures direct spectral solar radiation every 3

137 minutes across nine channels: 340nm, 380nm, 440nm, 500nm, 670nm, 870nm, 936nm, 1020nm,

138 and 1640nm. The measurement at the 936nm channel is used to retrieve the total atmospheric

139 water vapor content, while the remaining channels are used to derive aerosol optical depth (AOD)

140 with a retrieval error of approximately 0.01-0.02. Therefore, AERONET provides high-precision

141 aerosol characteristic parameters and can be used to validate satellite-retrieved AOD (Lu et al.,

142 2019). In this study, AOD measurements obtained from AERONET were used as ground truth to

143 verify the accuracy of satellite remote sensing retrievals. AERONET AOD data are categorized

144 into three quality levels: Level 1.0 (unscreened), Level 1.5 (cloud screened and quality controlled),

145 and Level 2.0 (quality assured). The study area primarily covers the Yangtze River Delta region,

146 where AERONET has several stations. However, continuous data were only available from the

147 Taihu and Xuzhou-CUMT stations, while data from other stations were relatively limited in

148 duration. Therefore, AERONET Level 1.5 AOD data with a large number of continuous and

149 current observations were selected for validating MISR AOD retrievals.

3. Methodology

3.1 Problems in the previous surface reflectance estimation method

The accurate estimation of surface reflectance is a crucial and challenging aspect in the retrieval of AOD from satellite remote sensing data (Remer et al., 2009; Gupta et al., 2016). Previous research has identified the variation patterns of 9-angle MISR AOD (Chen et al., 2021). However, the AOD retrieved at 9 angles exhibits relatively large errors when compared to AERONET AOD (Table S3). Atmospheric correction can eliminate the effects of clouds and aerosols on data, obtaining the true surface reflectance. When using the 6S model to calculate atmospheric correction reflectance for the MISR sensor, several parameters need to be inputted, including geometric parameters, AOD, aerosol types, sensor radiance data, and sensor altitude, etc. In this study, we inputted the MISR geometric parameters and radiation data corresponding to Taihu and Xuzhou-CUMT stations, while the AOD parameter inputted was the AERONET AOD for these two stations. Through the generated linear atmospheric correction formula, we calculated the atmospheric correction reflectance for each pixel. To investigate the reasons for the higher AOD values retrieved from the 9 MISR angles, this study compared the MISR atmospheric correction reflectance and MISR surface reflectance at the pixel location (Figure 1) (MISR surface reflectance calculation method referenced Chen et al. (2021)). It was observed that the MISR surface reflectance was relatively lower compared to the MISR atmospheric correction reflectance. As a result, the retrieved MISR AOD values were higher compared to AERONET AOD. Therefore, it is necessary to establish a correction model to adjust the MISR surface reflectance and improve the retrieval accuracy of MISR AOD.
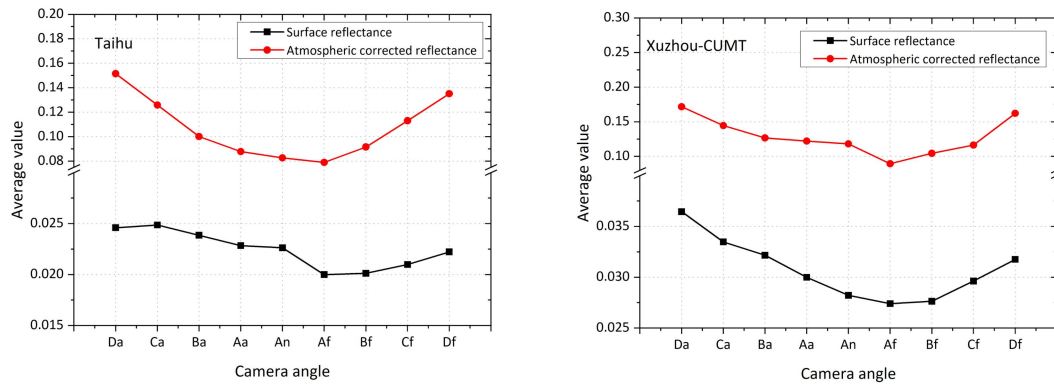
171   Figure 1. Comparison of MISR surface reflectance with atmospheric corrected reflectance in the

172   blue band (At the pixel locations of Taihu and Xuzhou-CUMT sites).

173   **3.2 Improved surface reflectance estimation method**

174   To develop a correction model that improves the surface reflectance, the design scheme of

175   this study is shown below:

176   (1) Calculation of MODIS atmospheric corrected reflectance

177   The atmospheric correction of MODIS L1B was carried out using the 6S model to obtain

178   MODIS atmospheric corrected reflectance. When using the 6S model to calculate the atmospheric

179   correction reflectance of the MODIS sensor, several parameters need to be provided, including

180   geometric parameters, AOD, atmospheric models, aerosol types, sensor radiance data, sensor

181   altitude, and spectral parameters. In this study, we used the MODIS geometric parameters and

182   radiance data corresponding to the Taihu and Xuzhou-CUMT sites. The AOD parameter was

183   obtained from the AERONET AOD data measured at these two sites. The atmospheric models

184   chosen were mid-latitude winter and mid-latitude summer to account for seasonal variations in

185   atmospheric transmission. The aerosol type selected was continental aerosol since it is typically

186   found in the Yangtze River Delta region. The sensor altitude was set to the height of satellite

187   observations. The spectral parameters were defined based on the wavelength bands of the MODIS

188 sensor. By providing these parameters, we can utilize the 6S model to calculate the atmospheric

189 correction reflectance of the MODIS sensor.

190 (2) Calculation of surface bidirectional reflectance

191 We utilized the MODIS BRDF/Albedo product MCD43A1 data and employed the Ross-Li

192 model to simulate surface bidirectional reflectance under MODIS and MISR observation

193 geometries. The linear kernel-driven BRDF model comprises three essential parameters: the

194 nadir-view reflectance, and the weighting coefficients for the two kernel functions. The model can

195 be computed using formulas 1-9.

196
$$BRDF(\theta_s,\theta_v,\phi) = f_{iso}(\Lambda) + f_{vol}(\Lambda)K_{vol}(\theta_s,\theta_v,\phi) + f_{geo}(\Lambda)K_{geo}(\theta_s,\theta_v,\phi) \tag{1}$$

197
$$K_{vol}(\theta_s,\theta_v,\phi) = \frac{(\pi/2-\xi)\cos\xi + \sin\xi}{\cos\theta_s + \cos\theta_v} - \frac{\pi}{4} \tag{2}$$

198
$$K_{geo}(\theta_s,\theta_v,\phi) = O(\theta_s,\theta_v,\phi) - \sec\theta'_s - \sec\theta'_v + \frac{1}{2}(1+\cos\xi')\sec\theta'_s \sec\theta'_v \tag{3}$$

199
$$O(\theta_s,\theta_v,\phi) = \frac{1}{\pi}(t - \sin t \cos t)(\sec\theta'_s + \sec\theta'_v) \tag{4}$$

200
$$\cos t = \frac{h}{b}\frac{\sqrt{D^2 + (\tan\theta'_s \tan\theta'_v \sin\phi)^2}}{\sec\theta'_s + \sec\theta'_v} \tag{5}$$

201
$$D = \sqrt{\tan^2\theta'_s + \tan^2\theta'_v - 2\tan\theta'_s \tan\theta'_v \cos\phi} \tag{6}$$

202
$$\cos\xi' = \cos\theta'_s \cos\theta'_v + \sin\theta'_s \sin\theta'_v \cos\phi \tag{7}$$

203
$$\theta'_s = \tan^{-1}(\frac{b}{r}\tan\theta_s) \tag{8}$$

204
$$\theta'_v = \tan^{-1}(\frac{b}{r}\tan\theta_v) \tag{9}$$

205 In the aforementioned equation, $BRDF(\theta_s,\theta_v,\phi)$ represents the bidirectional reflectance of

206 the surface, while θ_s, θ_v, and ϕ denote the solar zenith angle, view zenith angle, and relative

207 azimuth angle, respectively. Λ stands for the bandwidth, while $K_{vol}(\theta_s,\theta_v,\phi)$ and

208 $K_{geo}(\theta_s,\theta_v,\phi)$ represent the volumetric scattering kernel and geometric optical scattering kernel,

209   respectively. These terms are all functions of the incident and viewing angles. f_{iso}, f_{vol}, and

210   f_{geo} correspond to the weights assigned to isotropic scattering, volumetric scattering, and

211   geometric optical scattering in the reflectance, which serve as coefficients for their respective

212   kernel functions. ξ represents the scattering angle, while b, h, and r represent the vertical radius,

213   horizontal radius, and height of the sphere's center, respectively. Based on empirical values, these

214   three parameters can be considered as fixed values. Within the production process of MODIS

215   BRDF model parameter products, the following relationships exist among these parameters: h/b=2

216   and b/r=1 (Schaaf et al., 1999). By utilizing extrapolation with kernel functions, the surface's

217   bidirectional reflectance can be computed under arbitrary solar incident and satellite viewing

218   directions using the aforementioned equation.

219   (3) Improved calculation of surface reflectance by MISR

220   The new estimated MISR surface reflectance based on the MODIS atmospheric correction

221   was calculated by bringing the MODIS atmospheric correction reflectance into Eq. 10 and Eq. 11.

222   The MISR surface reflectance was combined with the newly estimated MISR surface reflectance,

223   and a regression was fitted (with 60% of the overall sample data randomly selected) to create a

224   surface reflectance error correction model, as shown in the following formula:

225

$$\rho(\theta_s, \theta_v, \phi)_{MISR\_a} = \rho(\theta_s, \theta_v, \phi)_{MODIS\_at} \times \frac{BRDF(\theta_s, \theta_v, \phi)_{MISR}}{BRDF(\theta_s, \theta_v, \phi)_{MODIS}} \tag{10}$$

226   In Eq. 10, $BRDF(\theta_s, \theta_v, \phi)_{MISR}$, $BRDF(\theta_s, \theta_v, \phi)_{MODIS}$ are BRDFs obtained at MISR and

227   MODIS angles, respectively. θ_s is the solar zenith angle, θ_v is the satellite zenith angle, and ϕ

228   is the relative azimuth angle. $\rho(\theta_s, \theta_v, \phi)_{MISR\_a}$ is the surface reflectance of MODIS at the

229   geometric observation angle of MISR, and $\rho(\theta_s, \theta_v, \phi)_{MODIS\_at}$ is the MODIS atmospheric

230   corrected reflectance.

231   This study selected spectral data containing 28 typical features of different types of

232 vegetation, soil and water bodies from five standard spectral libraries that come with the ENVI

233 software. The surface reflectance of different features in the blue bands of MODIS and MISR was

234 calculated using formulas (Chen et al., 2021).

235

$$\rho(\theta_s, \theta_v, \phi)_{MISR} = \rho(\theta_s, \theta_v, \phi)_{MISR\_a} \times 0.9834 - 0.0081 \tag{11}$$

236   The New MODIS surface reflectance ($\rho(\theta_s, \theta_v, \phi)_{MISR\_a}$) at the MISR angle obtained from

237 Eq. 11 is converted to the MISR surface reflectance by Eq. 11.

238   The MISR surface reflectance estimated by Eq. 11 is transformed using an error correction

239 model to obtain the final improved MISR surface reflectance. The improved MISR surface

240 reflectance will be used in the retrieval of the AOD. The MISR correction model was developed

241 by fitting a linear regression of the previously estimated MISR surface reflectance based on the

242 MODIS V5.2 algorithm to the MISR surface reflectance estimated based on the MODIS

243 atmospheric correction (60% of the data were randomly selected) as shown in Eq.12. The

244 previously estimated 9-angle MISR surface reflectance was error-corrected by Eq. 12 to obtain the

245 improved surface reflectance for the 9 angles of the MISR sensor, which was ultimately used to

246 perform the MISR AOD retrieval for the 9 angles.

247

$$\rho(\theta_s, \theta_v, \phi)_{MISR-b}{}^* = \rho(\theta_s, \theta_v, \phi)_{MISR} \times 0.9209 + 0.0409 \tag{12}$$

248   Where $\rho_{MISR-b}{}^*$ is the improved MISR surface reflectance in Eq. 12.

249 **3.3 Flow of improved multi-angle AOD retrieval**

250   The flow of the improved surface reflectance algorithm for this study is shown in Figure 2.

251 The MODISL1B data were first atmospherically corrected using 6S. Then, the MISR surface

252 reflectance estimated from previous study was combined with the new MISR surface reflectance

253 estimated from Eq. 11 to build a MISR error correction model for obtaining the improved MISR

254 surface reflectance (Chen et al., 2021). The study retrieved the MISR AOD for nine camera angles

255 using improved MISR surface reflectance. We validated the improved MISR AOD with

256 AERONET AOD. We compared the improved AOD with the previously retrieved AOD and

257 analyzed the accuracy and spatial distribution trends of the improved AOD. The AOD retrieval

258 method used in this study is based on chen et al. (2021). In our study, we used continental aerosols

259 for AOD retrieval and atmospheric correction using the 6S model. The selection of an appropriate

260 aerosol type is crucial for obtaining accurate aerosol optical depth. Previous studies have shown

261 that continental aerosols can be used to estimate aerosol optical depth in the Yangtze River Delta

262 region (He et al., 2015). We employed the same aerosol type for AOD retrieval and atmospheric

263 correction and utilized the 6S model for atmospheric correction. Thus, this study did not consider

264 the potential error propagation caused by aerosol type and atmospheric correction.
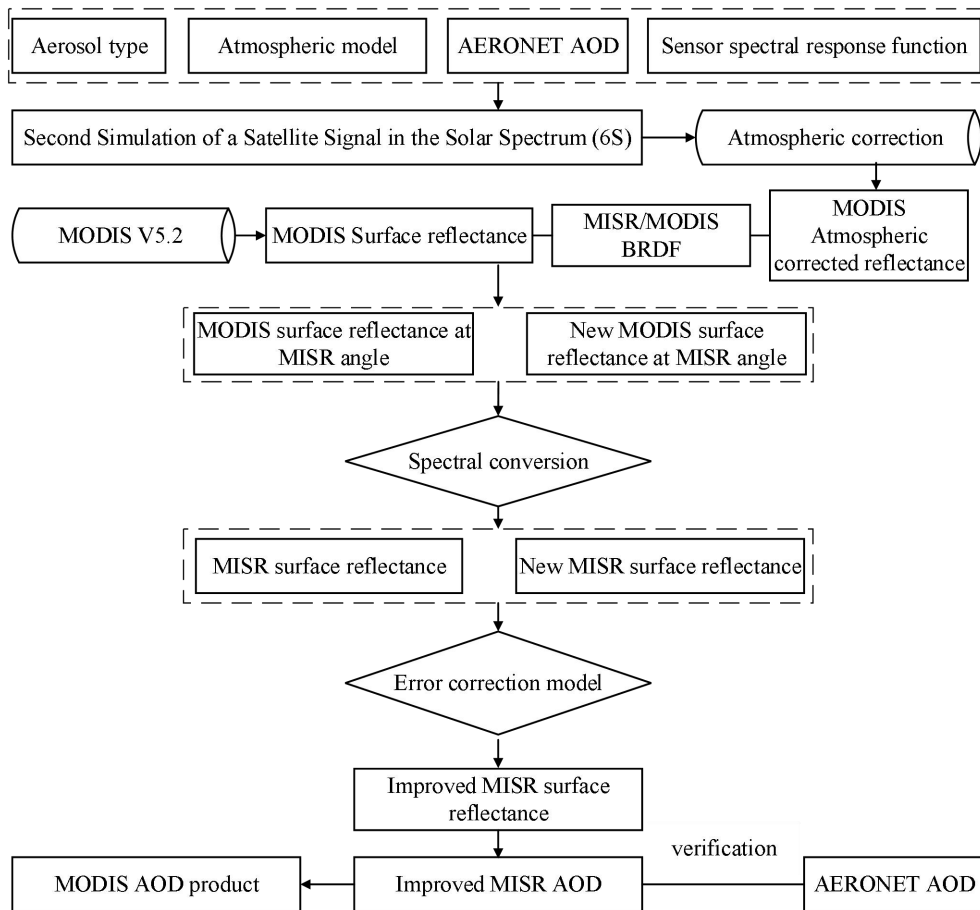
Figure 2. Flow chart of the improved MISR surface reflectance algorithm

4. Results and discussion

4.1 Improved MISR surface reflectance variation characteristics

The estimated MISR surface reflectance, the MISR atmospherically corrected reflectance, and the improved MISR surface reflectance are presented in Figure 3. These values represent the average of all sample data collected at the corresponding locations at the two sites, Taihu and Xuzhou-CUMT, during the valid dates of 2016-2018. It is worth noting that at both the Taihu and Xuzhou-CUMT sites, the nine-camera-angle MISR-improved surface reflectance values are generally higher than the MISR surface reflectance and lower than the MISR atmospherically corrected reflectance. The nine-camera-angle MISR surface reflectance values ranged from 0.02 to

276   0.04. On average, the improved surface reflectance values higher than the previously estimated

277   MISR surface reflectance.
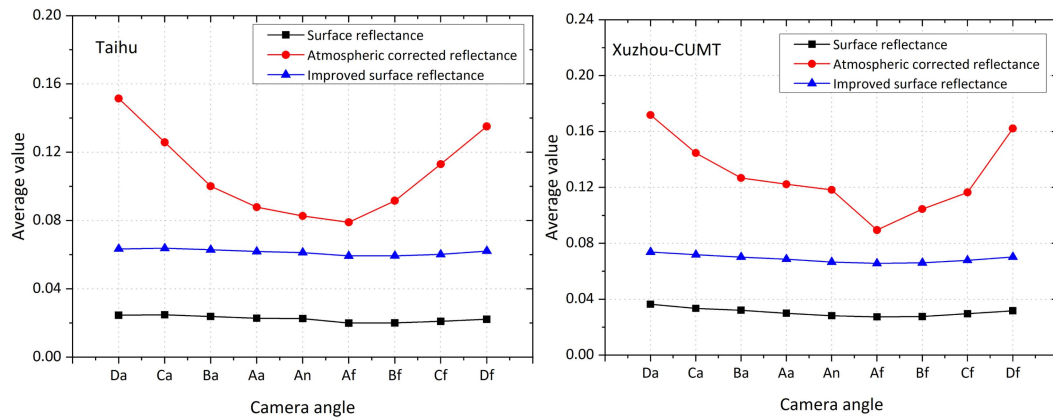
278   **Figure 3.** The comparison of MISR surface reflectance, atmospheric corrected reflectance and

279   improved surface reflectance in the blue band (This is the multi-year average of the sample data

280   for the two sites in Taihu and Xuzhou-CUMT).

281

282   To clarify the trend of the improved surface reflectance, the study conducted a time-series

283   analysis of the MISR surface reflectance and the improved surface reflectance (Figure 4). It is

284   evident from the analysis that the improved MISR surface reflectances are consistently higher than

285   the previously estimated MISR surface reflectances. The MISR surface reflectance values

286   generally range from 0-0.05, while the improved surface reflectance values range approximately

287   from 0.05-0.1. Overall, there has been an increase in the improved surface reflectance values.
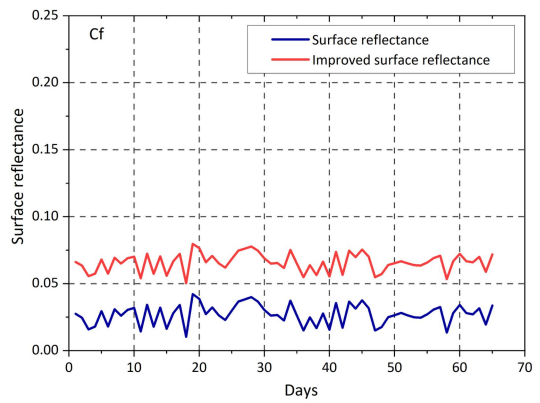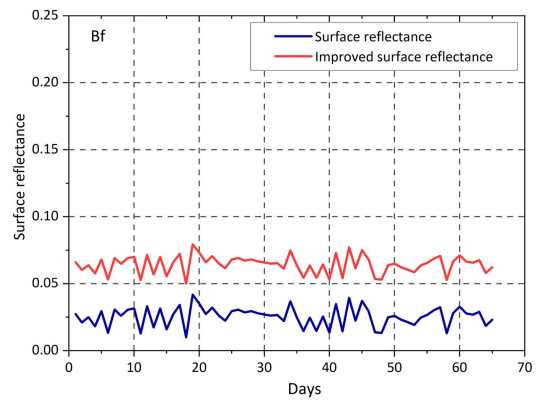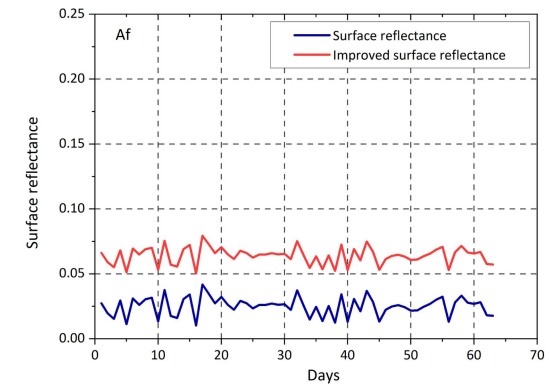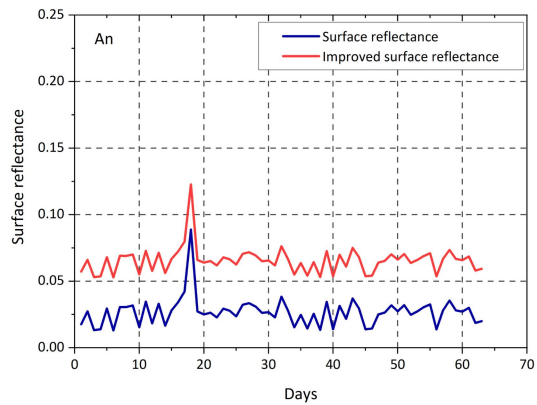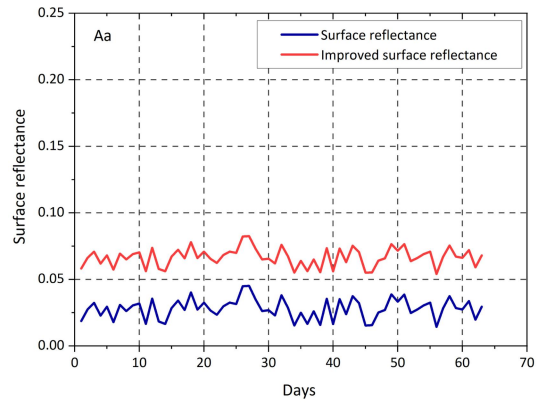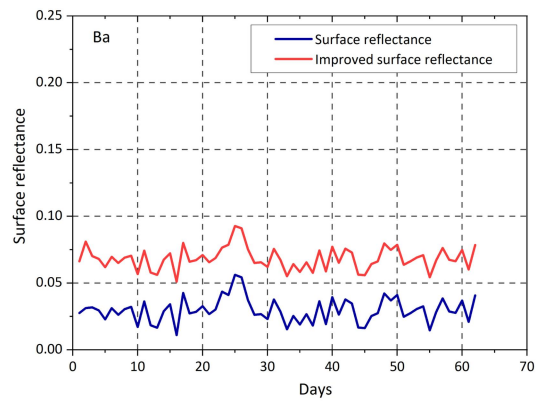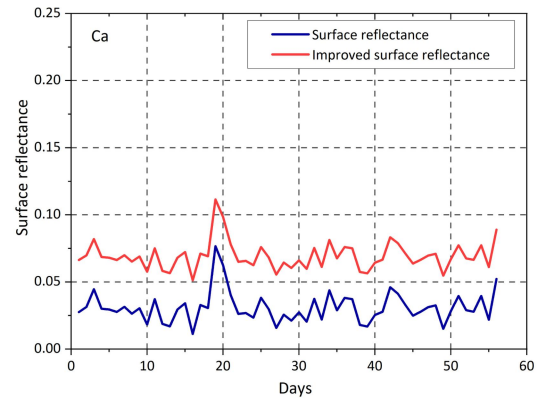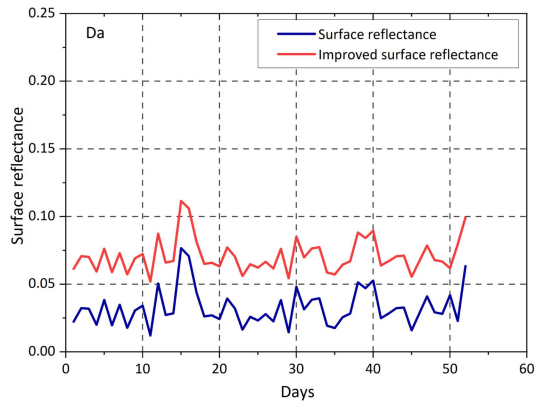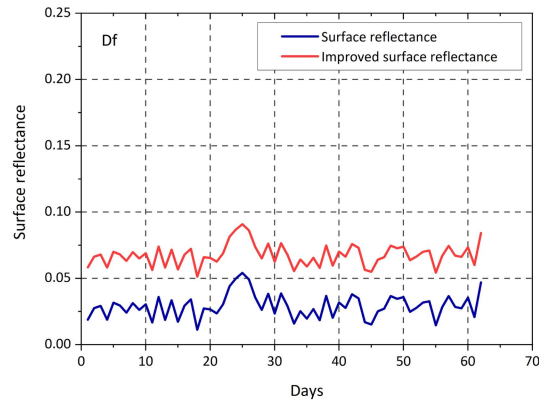
Figure 4. Surface reflectance time series of MISR sensors in the blue band at 9 observation angles.

(The order of time from front to back for 9 angles is shown in Table S2)

4.2 Results of the Improved MISR AOD retrieval

MISR AOD values for 2016-2018 were obtained using an improved surface reflectance retrieval. The study presents the retrieval results from nine camera observation angles of the MISR sensor on 12 June 2018 (Figure 5). From the spatial distribution of AOD, it is evident that the retrieval results in the study area do not exceed a value of 1. The overall spatial distribution trend is generally consistent with the results before the improvement (Chen et al., 2021), but there are differences in the magnitude of the values. Values in the north-eastern and southern regions range from 0.5 to 1, indicating poor air quality to some extent in these areas. The AOD values retrieved from the five camera observation angles, Ba, Aa, An, Af, and Bf, fall within the approximate range of 0.25-0.5. In the central region, the AOD values from the four camera observation angles, Da, Ca, Cf, and Df, are mostly in the range of 0-0.25. The values suggest that the air quality in the central region is generally good, with some areas experiencing light air pollution. The higher AOD in the southern part of Shandong Province and the northern part of Jiangsu Province may be attributed to increased local aerosol emissions resulting from human activities.
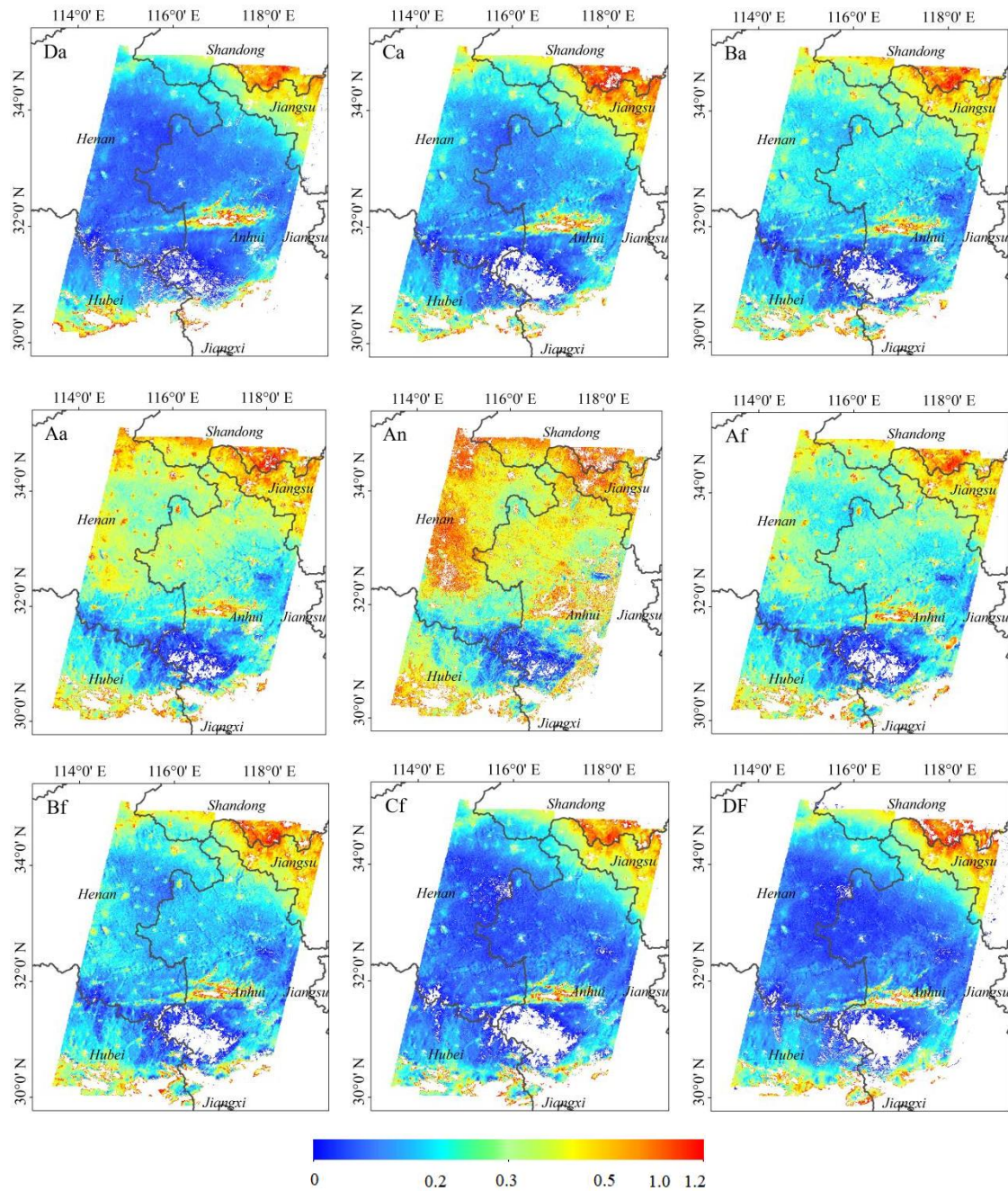
Figure 5. Plot of AOD 550nm retrieval results for the improved MISR 9 camera angles on 12 June 2018.

The study validates our improved MISR AOD spatial distribution results by comparing them with MODIS AOD products on the same date (Figure 6). The MODIS AOD products have a resolution of 3km. It can be observed that the trend of the spatial distribution of MODIS AOD products is consistent with the improved MISR AOD. However, the MODIS AOD product has

310   more missing data, which can be avoided by using AOD obtained from the retrieval of the

311   improved algorithm. Additionally, the AOD retrieval through the improved algorithm has a higher

312   resolution when compared to the image quality of the MISR AOD product.
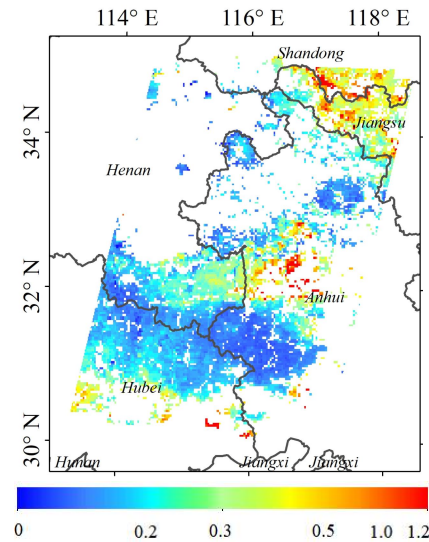
313   **Figure 6**. MODIS AOD 550nm product spatial distribution on June 12, 2018

314   **4.3 Verification of the improved MISR AOD**

315   There are many AERONET sites in the Yangtze River Delta region, but currently, only the

316   Taihu and Xuzhou-CUMT sites continue to provide data, and other sites have a limited time frame

317   for obtaining data. Therefore, the Taihu and Xuzhou-CUMT sites, which have more data, were

318   selected for verification. To verify the retrieved MISR AOD, we selected effective AOD records

319   in the 550nm band within a 30-minute interval between the AERONET ground observation site

320   and the Terra satellite. The 9 camera views of MISR require approximately 7 minutes to observe

321   the same geographical location, with relatively short intervals. Therefore, we used the calculated

322   AERONET AOD average as the approximate truth value and compare it with the retrieved MISR

323   AOD to verify and reduce errors caused by time difference. In terms of space, we selected pixels

324   observed by the MISR sensors from 9 angles and compared them with the nearest data observed

325   by AERONET, which can reduce errors caused by spatial differences. As the solar photometer

326   does not have a 550nm wavelength that corresponds to the retrieval results, the AOD at 550nm

327   was calculated by applying Angstrom (Eq. 13).

328

$$\tau(\lambda) = \beta\lambda^{-\alpha} \tag{13}$$

329   In the formula, $\tau(\lambda)$ is the AOD at wavelength λ, β is the concentration of the entire

330   atmospheric aerosol, and α is the wavelength index of Angstrom.

331   In this study, four parameters will be used to assess the accuracy of the remotely sensed AOD

332   dataset, namely the correlation coefficient (R), the root mean square error (RMSE), p-value and

333   the relative mean bias (RMB). The specific calculation principles for the three parameters R,

334   RMSE and RMB are shown in Eq. 14-16. The validation results of this study's improved AOD

335   dataset from 2016-2018 at Taihu and Xuzhou-CUMT sites are shown in Figure 7 and Figure 8.

336   In general, the scatter plot is distributed above and below the 1:1 line. R is a parameter used

337   to characterize the correlation between the remote sensing retrieval results and the ground-based

338   retrieval results. At the Taihu site, R reach up to 0.89, and at the Xuzhou-CUMT site, R reach up

339   to 0.85. The RMSE is a parameter used to characterize the absolute error of the remote sensing

340   retrieval results, with a minimum root mean square error of 0.21 at the Taihu site and 0.20 at the

341   Xuzhou-CUMT site. RMB is the parameter used to characterize the relative error of the remote

342   sensing retrieval results, with a minimum RMB of 0.52 at the Taihu site and 0.32 at the

343   Xuzhou-CUMT site. In summary, by comparing the results with the validation of the AOD scatter

344   plot before the improvement, the accuracy of the nine camera observation angles at both sites has

345   improved after the improvement (Table 1). In Table 1, R represents the correlation between the

346 old AOD retrieval results and AERONET AOD. RMB represents the relative deviation between

347 the old algorithm-retrieved AOD and AERONET AOD. Improved R represents the correlation

348 between the improved AOD retrieval results and AERONET AOD. Improved RMB represents the

349 relative deviation between the AOD retrieved using the improved algorithm and AERONET

350 AOD.

351
$$R = \frac{\sum_{i=1}^{N}(A_i - \overline{A})(A_i' - \overline{A'})}{\sqrt{\sum_{i=1}^{N}(A_i - \overline{A})^2 \sum_{i=1}^{N}(A_i' - \overline{A'})^2}} \tag{14}$$

352
$$RMSE = \sqrt{\sum_{i=1}^{N}(A_i - A_i')^2 / N} \tag{15}$$

353
$$RMB = \sum_{i=1}^{N}(A_i - A_i') / N \tag{16}$$

354 where A_i is the retrieve MISR AOD, A_i' is the corresponding AERONET AOD, $\overline{A}$

355 and $\overline{A'}$ are the mean values of the retrieve MISR AOD and AERONET AOD, respectively. N is

356 the number of valid matching results for AERONET AOD and MISR AOD.
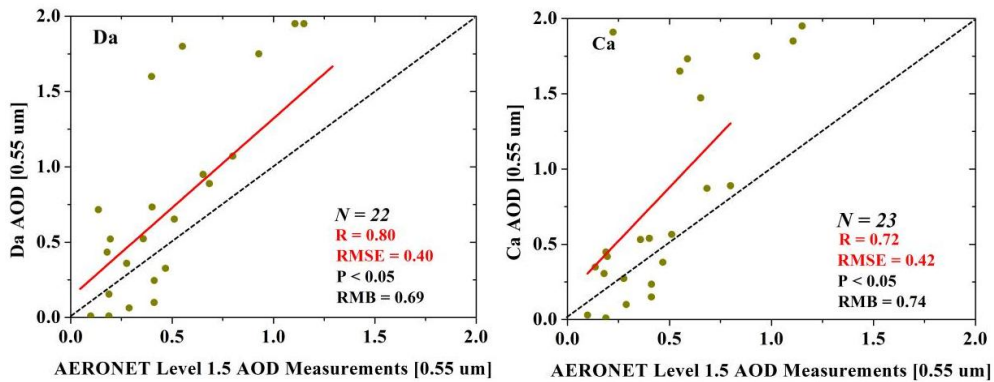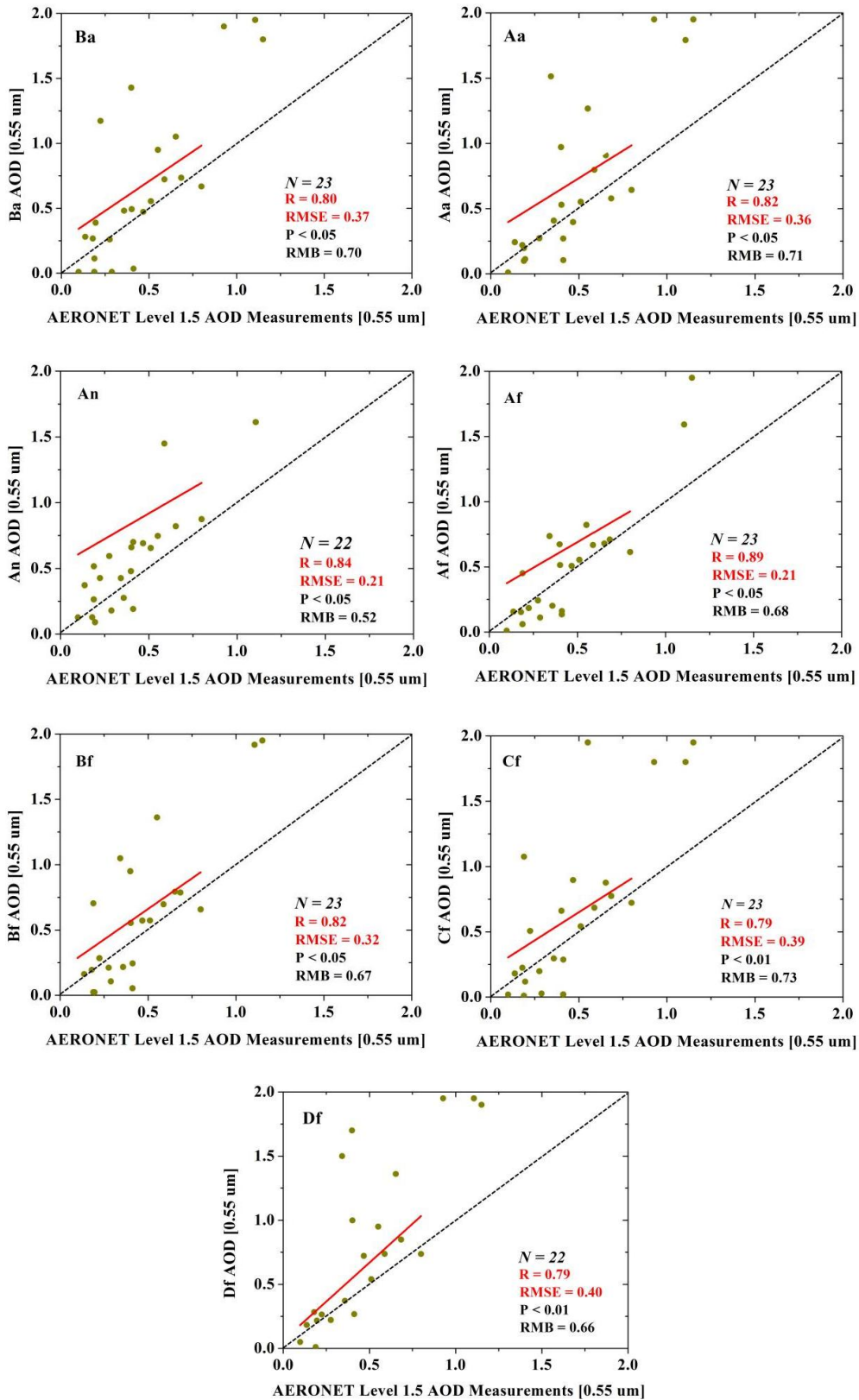
 Figure 7. Comparison between improved MISR AOD and AERONET AOD at Taihu site (N is

 the number of verification points, red line represents a linear fitting line).
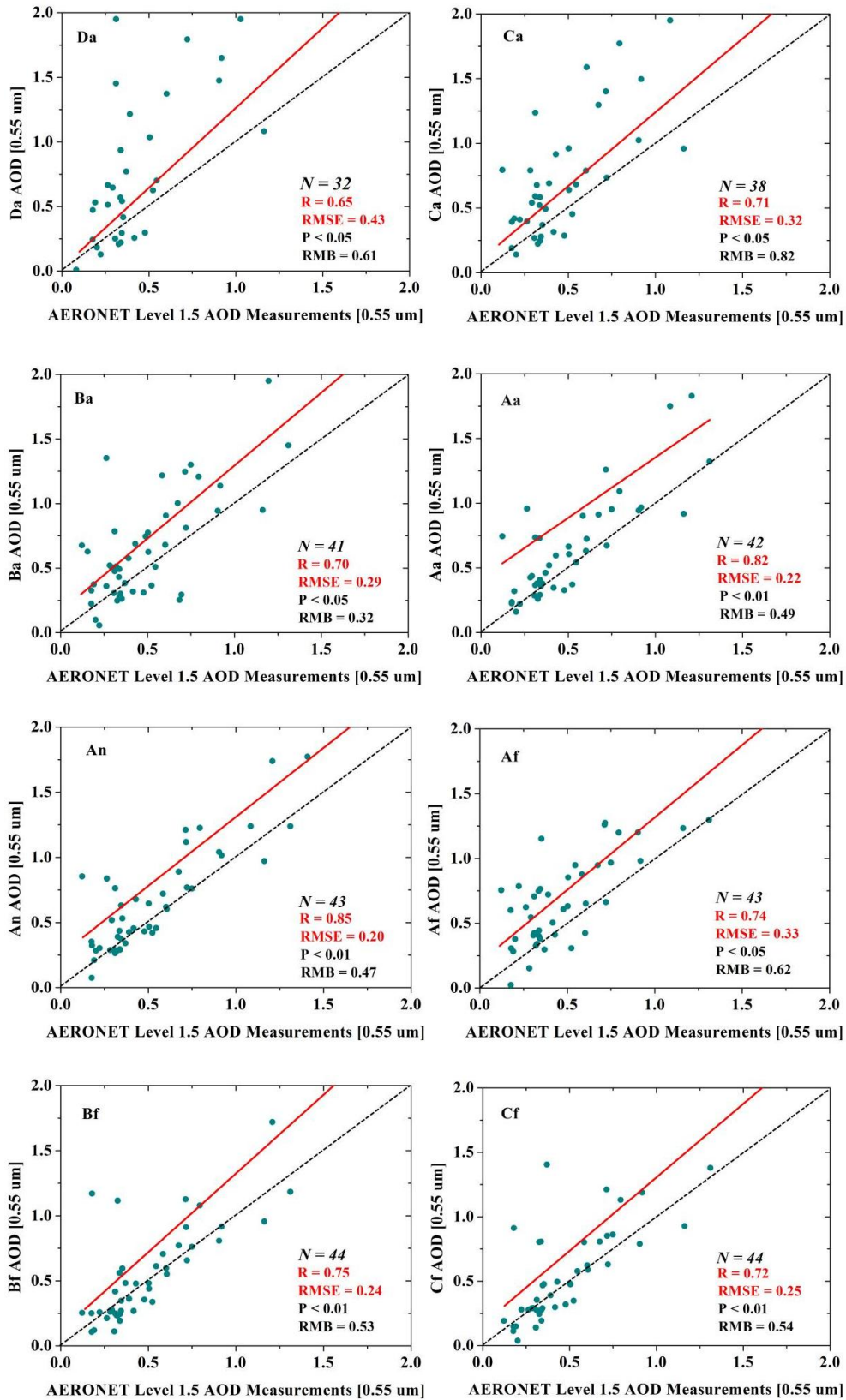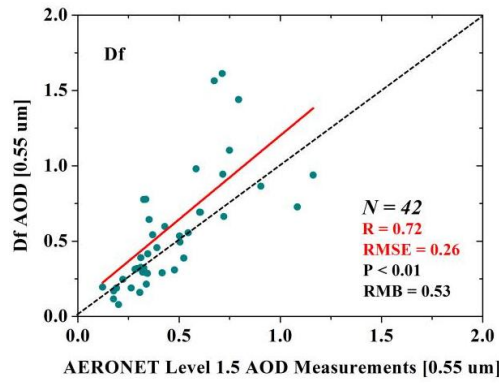
 Figure 8. Comparison between improved MISR AOD and AERONET AOD at Xuzhou-CUMT

 site (N is the number of verification points, red line represents a linear fitting line).
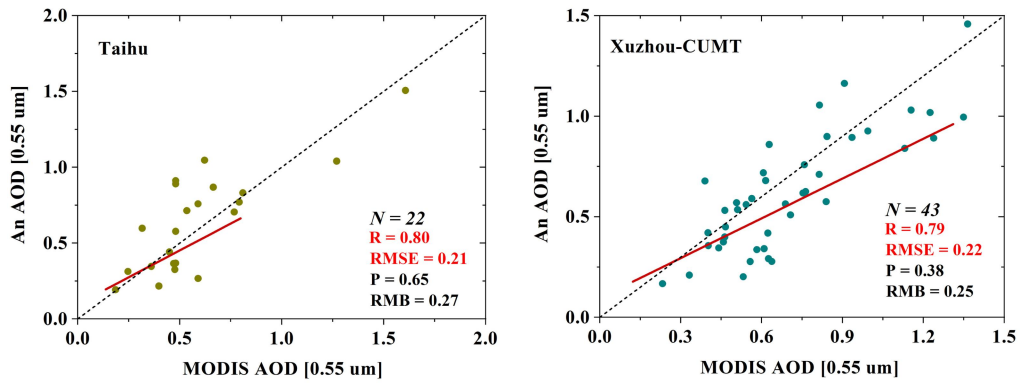
 Figure 9. Comparison of validation of retrieved AOD with MODIS AOD product

 Table 1. Precision comparison of MISR AOD and AERONET AOD before

 and after improvement

Site	Angle	R	RMB	Improved R	Improved RMB
	Da	0.77	1.08	0.80	0.69
	Ca	0.70	1.00	0.72	0.74
	Ba	0.77	0.61	0.80	0.70
	Aa	0.81	0.68	0.82	0.71
Taihu	An	0.45	1.22	0.84	0.52
	Af	0.72	0.87	0.89	0.68
	Bf	0.72	0.60	0.82	0.67
	Cf	0.57	0.65	0.79	0.73
	Df	0.77	0.47	0.79	0.66
Xuzhou-	Da	0.45	1.58	0.65	0.61

CUMT	Ca	0.59	0.96	0.71	0.82
	Ba	0.67	0.78	0.70	0.32
	Aa	0.73	0.78	0.82	0.49
	An	0.75	0.85	0.85	0.47
	Af	0.72	0.63	0.74	0.62
	Bf	0.62	0.65	0.75	0.53
	Cf	0.68	0.66	0.72	0.54
	Df	0.67	0.65	0.72	0.53

365

366   By comparing the validation results of MODIS AOD products with those of observation sites

367   (Taihu: R=0.59, RMSE=0.19, P<0.05, RMB=0.52; Xuzhou-CUMT: R=0.71, RMSE=0.25, P<0.05,

368   RMB=0.44) (Chen et al., 2021), we find that the improved MISR AOD has a higher correlation

369   with MODIS AOD products in the Taihu and Xuzhou-CUMT sites. The smaller observation angle

370   of the improved MISR AOD, the closer the error is to that of the MODIS AOD product. The

371   observation angle of MISR An is the same as that of MODIS. Therefore, we selected An

372   observation angle and MODIS AOD products at two pixel positions in Taihu and Xuzhou-CUMT

373   for verification (Figure 9). The results show that the An AOD retrieval by the improved algorithm

374   correlates well with the MODIS AOD product, and the position errors of the two image elements

375   are close to each other. The RMSE of the Xuzhou-CUMT site is slightly higher than that of Taihu

376   site, and the RMB of Taihu site is slightly higher than that of the Xuzhou-CUMT site.

377   **5. Conclusion**

378   This study first explored the problem of estimating the surface reflectance in our previous

379   study. We obtained an error correction model for surface reflectance by using a linear fit of the

380   MISR surface reflectance and a new estimate of the MISR surface reflectance. The improved

381   MISR surface reflectance was obtained through the error correction model. We then retrieved a

382   new AOD product using the improved surface reflectance and a lookup table constructed from the

383   6S model. Two AERONET ground observation sites with longer time series were used to validate

384   the AOD obtained by satellites.

385   (1) Overall, the improved AOD and its spatial distribution trends are consistent with our

386   previous results. The AOD estimated by our improved method exhibited higher accuracy and a

387   high degree of agreement with the AERONET ground-based observational AOD.

388   (2) More importantly, compared to the MODIS AOD products, the retrieved AOD in this

389   study has fewer missing AOD pixels and finer spatial resolution. The retrievals of An AOD by the

390   improved algorithm are highly correlated with the MODIS AOD products, as shown through

391   validation with the MODIS AOD product.

392   (3) In the future, more aerosol models that conform to the actual situation in the study area

393   can be constructed using the AERONET ground observation data and introduced into the MISR

394   AOD retrieval algorithm to further improve the accuracy of the AOD retrieval results. In this study,

395   the AERONET AOD was used as the true value and as an input for the AOD parameter in the 6S

396   model for atmospheric correction of MISR and MODIS images. We then obtained a surface

397   reflectivity error correction model to retrieve the AOD for the entire region. It should be

398   emphasized that the more AERONET sites used to train the corrected model, the more accurate

399   the AOD results obtained by this method. However, the data from the AERONET ground

400   observation sites were limited. In the future, the study area can be expanded on a large scale and

401   for a longer time series.

402   **Acknowledgement**

403   This study was supported by the Key Program of the National Natural Science Foundation of

404   China (42130609), Jiangsu Funding Program for Excellent Postdoctoral Talent (2023ZB482), the

405   Natural Science Foundation of Jiangsu Province of China (BK20220455), and the National

406   Science Foundation of China (42201028).

407   **Competing interests**

408   The contact author has declared that none of the authors has any competing interests.

Reference

Berhane, S. A.; Bu, L. Aerosol-Cloud Interaction with Summer Precipitation over Major Cities in
    Eritrea[J]. Remote Sens-basel, 2021, 13(4):21.

Chen, L.; Wang, R.; Han J. Influence of observation angle change on satellite retrieval of aerosol
    optical depth[J]. Tellus B, 2021, 73.

Chen, L.; Fei, Y.; Wang, R. Retrieval of high temporal resolution aerosol optical depth using the
    GOCI remote sensing data[J]. Remote Sens-basel. 2021, 13:2376.

Chen, L.; Wang, R.; Wei, G. A surface reflectance correction model to improve the retrieval of
    MISR aerosol optical depth supported by MODIS data[J]. Adv Space Res, 2021,
    67(2):858-867.

Dao, Y.; Gong, W. Observed holiday aerosol reduction and temperature cooling over East Asia[J].
    J Geophys Res-atmos, 2014.

Daniel, R.; Steven, S.; Robert, W.; Leo, D. Climate Effects of Aerosol-Cloud Interactions[J].
    Science, 2014, 343, 379-380.

Dehghani, M.; Saeedi, A. A.; Zamanian, Z. A study of the relationship between indoor and outdoor
    particle concentrations in Hafez hospital in Shiraz[J]. Phys.Rev.C, 2012.

Dong, W.; Tao, M.; Xu, X.; Wang, J.; Wang, Y.; Wang, L.; Song, Y.; Fan, M.; Chen, L. Satellite
    Aerosol Retrieval From Multiangle Polarimetric Measurements: Information Content and
    Uncertainty Analysis," IEEE Trans. Geosci. Remote Sens. 2023, 61, 1-13.

Dubovik, O.; Li.; Mishchenko M. I. Polarimetric remote sensing of atmospheric aerosols:
    Instruments, methodologies, results, and perspectives[J]. Pergamon, 2019, 474-511.

Deuzé, J. L.; Bréon, F. M.; Devaux, C.; Goloub, P.; Herman, M.; Lafrance, B.; Maignan, F.;

431   Marchand, A.; Nadal, F.; Perry, G.; Tanré, D. Remote sensing of aerosols over land surfaces

432   from POLDER-ADEOS-1 polarized measurements. J Geophys Res-atmos, 2001, 106(D5):

433   4913-4926.

434   Flowerdew, R. J.; Haigh, J. D. Retrieval of aerosol optical thickness over land using the ATSR-2

435   Dual-look Satellite Radiometer. Geophys Res. Lett. 1996, 23 (4): 351-354.

436   Giles, D. M.; Sinyuk, A.; Sorokin, M. G. Advancements in the Aerosol Robotic Network

437   (AERONET) Version 3 database-automated near-real-time quality control algorithm with

438   improved cloud screening for Sun photometer aerosol optical depth (AOD) measurements[J].

439   Copernicus GmbH, 2019, 12(1), 169-209.

440   Gupta, P.; Levy, R. C.; Mattoo, S. A surface reflectance scheme for retrieving aerosol optical depth

441   over urban surfaces in MODIS dark target retrieval algorithm[J]. Atmos Meas Tech, 2016,

442   9(7): 3293-3308.

443   Hatzianastassiou, N. The direct effect of aerosols on the radiation budget and climate of the

444   Earth-atmosphere system: its variability in space and time. EGU General Assembly

445   Conference Abstracts EGU General Assembly Conference Abstracts, 2009.

446   Holben, B. N.; Tanré, D.; Smirnov, A. An emerging ground-based aerosol climatology: Aerosol

447   optical depth from AERONET[J]. J Geophys Res, 2001, 106, 12067-12097.

448   Huang X , Ding A .Aerosol as a critical factor causing forecast biases of air temperature in global

449   numerical weather prediction models[J].Science Bulletin,

450   2021.DOI:10.1016/j.scib.2021.05.009.

451   Hsu, N. C.; Tsay, S. C.; King, M. D. Aerosol properties over bright-reflecting source regions[J].

452   IEEE Trans. Geosci. Remote Sens, 2004, 42(3):557- 569.

453 Kaufman, Yoram J. The MODIS 2.1-um channel--correlation with visible reflectance for use in

454   remote sensing of aerosol.[J]. IEEE T Geosci Remote, 1997, 35, 1286-1298.

455 Kokhanovsky, A. A.; Curier, R. L.; Leeuw, G. D.; Grey, W. M. F. The intercomparison of AATSR

456   dual-view aerosol optical thickness retrievals with results from various algorithms and

457   instruments. Int. J. Remote Sens. 2009, 30 (17): 4525-4537.

458 Lee, S. S.; Donner L. J.; Penner J. E. Thunderstorm and stratocumulus: How does their contrasting

459   morphology affect their interactions with aerosols?[J]. Atmos. Chem. Phys. 2010, 10(2),

460   6819-6837.

461 Li, E.; Zhang, Z.; Tan, Y. A Novel Cloud Detection Algorithm Based on Simplified Radiative

462   Transfer Model for Aerosol Retrievals: Preliminary Result on Himawari-8 Over Eastern

463   China[J]. IEEE T Geosci Remote, 2020, 59(3):1-12.

464 Li, Y.; Xue, Y.; Guang, J. Ground-Level PM2.5 Concentration Estimation from Satellite Data in

465   the Beijing Area Using a Specific Particle Swarm Extinction Mass Conversion Algorithm[J].

466   Remote Sens-basel, 2018, 10(12), 1906.

467 Lu, S.; Xue, Y.; Yang, X.-H.; Leys, J.; Guang, J.; Che, Y.-H.; Fan, C.; Xie, Y.Q.; Li, Y. Joint

468   Retrieval of Aerosol Optical Depth and Surface Reflflectance Over Land Using

469   Geostationary Satellite Data. IEEE Trans. Geosci. Remote Sens. 2019, 57, 1489–1501.

470 Mironova, I. A. Aerosols over continental Portugal (1978-1993): their sources and an impact on

471   the regional climate[J]. Atmos. Chem. Phys. 2015, 15(11):6407-6418.

472 Remer, L. A; Tanré, D.; Kaufman, Y. J. Algorithm for remote sensing of tropospheric aerosol from

473   MODIS: Collection 005[J]. 2009.

474 Samset, B. H.; Sand, M.; Smith, C. J. Climate Impacts From a Removal of Anthropogenic Aerosol

475   Emissions[J]. Geophys Res Lett, 2018, 45(2).

476   Sun, E.; Fu, C.; Yu, W. Variation and Driving Factor of Aerosol Optical Depth over the South

477   China Sea from 1980 to 2020[J]. Atmosphere, 2022, 13, 372.

478   Sundstrom, A. M.; Kolmonen, P.; Sogacheva, L.; Leeuw, G. D. Aerosol retrieval over China with

479   the AATSR dual view algorithm. Remote Sens. Environ. 2012, 116 (1): 189-198.

480   Xie, Y.; Xue, Y.; Jie, G. Deriving a Global and Hourly Data Set of Aerosol Optical Depth Over

481   Land Using Data From Four Geostationary Satellites: GOES-16, MSG-1, MSG-4, and

482   Himawari-8[J].IEEE T Geosci Remote, 2019, 99:1-12.

483   Zhang, Y.; Li, Z.; Liu, Z. Retrieval of aerosol fine-mode fraction over China from satellite

484   multiangle polarized observations: validation and comparison[J]. Atmos Meas Tech, 2021, 2,

485   1655-1672.